



Discrete element calculations of the impact of a sand column against rigid structures

S.M. Pingle^a, N.A. Fleck^a, H.N.G. Wadley^b, V.S. Deshpande^{a,*}

^aDepartment of Engineering, University of Cambridge, Trumpington Street, Cambridge CB2 1PZ, UK

^bDepartment of Materials Science & Engineering, University of Virginia, Charlottesville, VA 22904, USA

ARTICLE INFO

Article history:

Received 12 February 2011

Accepted 31 October 2011

Available online 4 December 2011

Keywords:

Fluid-structure interaction

Discrete element simulations

Blast

Landmines

ABSTRACT

Discrete particle simulations of column of an aggregate of identical particles impacting a rigid, fixed target and a rigid, movable target are presented with the aim to understand the interaction of an aggregate of particles upon a structure. In most cases the column of particles is constrained against lateral expansion. The pressure exerted by the particles upon the fixed target (and the momentum transferred) is independent of the co-efficient of restitution and friction co-efficient between the particles but are strongly dependent upon the relative density of the particles in the column. There is a mild dependence on the contact stiffness between the particles which controls the elastic deformation of the densified aggregate of particles. In contrast, the momentum transfer to a movable target is strongly sensitive to the mass ratio of column to target. The impact event can be viewed as an inelastic collision between the sand column and the target with an effective co-efficient of restitution between 0 and 0.35 depending upon the relative density of the column. We present a foam analogy where impact of the aggregate of particles can be modelled by the impact of an equivalent foam projectile. The calculations on the equivalent projectile are significantly less intensive computationally and yet give predictions to within 5% of the full discrete particle calculations. They also suggest that “model” materials can be used to simulate the loading by an aggregate of particles within a laboratory setting.

© 2011 Elsevier Ltd. All rights reserved.

1. Introduction

The impact of high velocity, granular media upon an engineering structure is encountered in a wide variety of situations such as rock slide, avalanche, hail impact and the detonation of shallow buried explosives (land mines). While single particle impact is now well understood, the collective behaviour of densely concentrated, high velocity particles is not well established, and impedes the design of protective systems. The granular assembly can be viewed as a set of discrete particles or as an effective medium. We know from recent work that sandwich structures with a cellular metal core have a significantly higher resistance to blast loads compared to monolithic structures of equal mass; see for example Fleck and Deshpande [1] and Liang et al. [2]. This improved performance is greatest for impulsive loads applied by water and primarily stems from that fact that sandwich structures acquire only a small fraction of the incident impulse (Deshpande et al. [3]; Wei et al. [4]) as a result of fluid-structure interaction

(FSI). The extension of these ideas to the design of structures against soil impact from say a landmine explosion (see Fig. 1) requires a better understanding of the dynamic interaction of soils with structures; the development of such an understanding from a particle-based perspective is the focus of this article.

For the landmine problem schematically illustrated in Fig. 1, there are three sequential phases: (i) The transfer of impulse from the explosive to surrounding soil and the formation of a dispersion of high velocity particles, (ii) the propagation (with spreading) of the expanding soil ejecta and (iii) impact of the soil ejecta with the structure leading to momentum transfer to the protection system (i.e. the soil-structure interaction). Direct experimental characterizations of buried explosive events are essential for getting a better understanding of the complex phenomena accompanying landmine blasts. Such experimental studies [5–7] have led to the development of empirical models to quantify the impulsive loads generated by landmines [8] and thereby to the construction of design-for-survivability codes [9]. However, these empirical approaches are restricted to the situations under which they were developed and cannot be extrapolated to different soil types and to the sandwich type systems sketched in Fig. 1. A predictive modelling capability is required in order to extend existing knowledge.

* Corresponding author. Tel.: +44 1223 332664.

E-mail address: vsd@eng.cam.ac.uk (V.S. Deshpande).

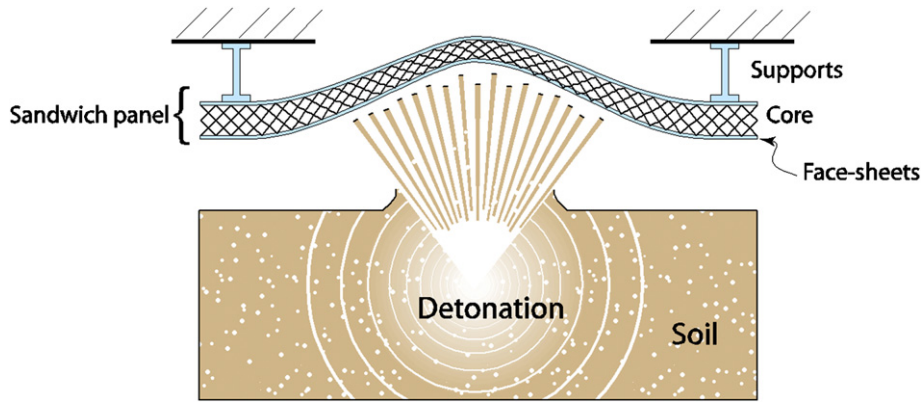


Fig. 1. Sketch of a prototypical problem of a clamped sandwich structure loaded by a shallow mine explosion.

There have been numerous attempts at developing constitutive models for soils under extreme dynamic loading with the eventual aim of employing these models in coupled Eulerian and Lagrangian numerical codes to predict the structural response to landmines. Readers are referred to Johnson [10] for a review of soil models used in explosive excavation and Gruzicic et al. [11,12] for a detailed analysis of soil models used to simulate landmine explosions. Notable among these are the so-called three phase model of Wang et al. [13,14] which is a modified Drucker–Prager [15] model and the porous-material/compaction model developed by Laine and Sandvik [16]. The porous-material/compaction model is widely used in military design codes but has the drawback that it does not account for the effect of moisture content. Gruzicic et al. [11] have modified the Laine and Sandvik [16] model to include the effect of moisture and illustrated its applicability by comparing predictions of blast impulse with data from Bergeron and Tremblay [17]. Discrepancies between measurements and predictions persist.

The soil models listed above are restricted to a regime where the packing density of the soil is sufficiently high that the particle–particle contacts are semi-permanent. While these models are appropriate during the initial stages of a buried explosion or during an avalanche or land slide, their applicability when widely dispersed particles impact a structure is questionable [18]. Deshpande et al. [19] modified a constitutive model of Bagnold [20] to develop a continuum soil model applicable to soils in both their densely packed and dispersed states. However, the successful implementation of this model within a coupled Eulerian and Lagrangian (CEL) computational framework has been elusive because of well known computational problems during the analysis of low density particle sprays; see Wang et al. [13] for a discussion of these numerical issues.

Here, we use an alternative approach to modelling the sand-structure interaction: low density soil is treated as an aggregate of particles, and the contact law between the particles dictates the overall aggregate behaviour. This approach has several advantages: (i) there is no need to make a-priori assumptions about the constitutive response of the aggregate (this becomes an outcome of the simulations), (ii) it provides a fundamental tool to study the essential physics of the sand-structure interaction and (iii) given that the sand is represented by a discrete set of particles we do not face the usual numerical problems associated with solving for the equivalent continuum descriptions. In this initial study we restrict out attention to understanding the sand-structure interaction (SSI) of a column of particles with both rigid-fixed and rigid-free targets. This rather idealised but fundamental fluid-structure interaction (FSI) problem is the “sand-blast” analogue to the classical water-blast FSI problem as studied by Taylor [21], and is intended to

provide the theoretical underpinning for more complex three-dimensional problems.

2. The discrete element methodology

The discrete element calculations were performed using the GRANULAR package in the multi-purpose molecular dynamics code LAMMPS [22]. Two-dimensional calculations were conducted with circular cylindrical particles of diameter D lying in the $x_1 - x_2$ plane (and with a thickness b in the prismatic out-of-plane x_3 -direction). Subsequently, these particles will be referred to as sand particles. The granular package in LAMMPS is based on the soft-particle contact model introduced by Cundall and Strack [23] and extended to large scale simulations by Campbell and co-workers [24,25]. A schematic of the soft-particle contact model is shown in Fig. 2 and comprised a linear spring with spring constant K_n and linear dashpot with damping constant γ_n , governing the normal motion and a linear spring of spring constant K_s and Coulomb friction co-efficient μ , governing the tangential motion during the contact of two identical particles of mass m_p . Define unit vectors \hat{e}_n and \hat{e}_s such that \hat{e}_n is in the direction of the outward normal to the particles along the line connecting the centres of the two particles and $\hat{e}_n \times \hat{e}_s$ is a unit vector in the x_3 direction. The force acting on each particle is then given as

$$F = \begin{cases} F_n \hat{e}_n - F_s \hat{e}_s & \text{if } \delta_n \leq 0 \\ 0 & \text{otherwise} \end{cases} \quad (1)$$

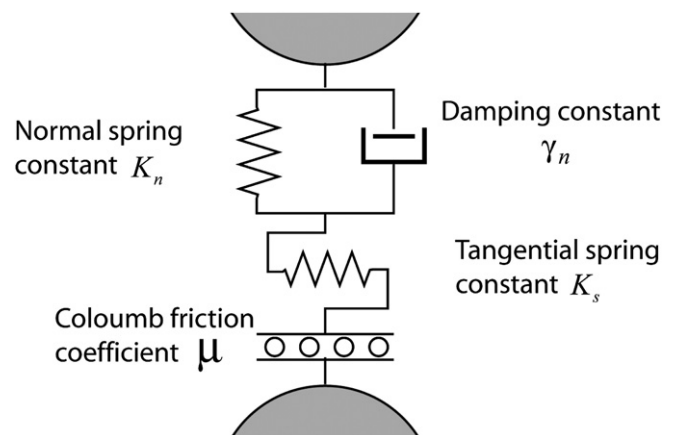


Fig. 2. Sketch illustrating the contact law between two particles in the discrete calculations.

where r is the distance between the particle centres and $\delta_n = r - D$ is the interpenetration. The normal force is given as

$$F_n = K_n \delta_n + m_{\text{eff}} \gamma_n \dot{\delta}_n \quad (2)$$

where m_{eff} is the effective or reduced mass of the two contacting bodies. In the calculations presented here impacts were either between particles or between particles and laterally confining (boundary) walls with $m_{\text{eff}} = m_p/2$ and m_p in these two cases, respectively. It now remains to specify the tangential force F_s . Define $\dot{\delta}_s$ as the tangential displacement rate between the contacting particles. We then stipulate F_s via an “elastic–plastic” relation so as to simulate Coulomb friction, i.e.

$$\dot{F}_s = \begin{cases} K_s \dot{\delta}_s & \text{if } |F_s| < \mu |F_n| \text{ or } F_s \dot{\delta}_s < 0 \\ 0 & \text{otherwise} \end{cases} \quad (3)$$

As discussed by Bathurst and Rothenburg [26] the Poisson’s ratio of the solid material of the particles is related to the ratio K_s/K_n , while K_n scales with the Young’s modulus of the solid. The damping constant γ_n , determines the loss of energy during normal collisions and thereby dictates the co-efficient of restitution e . Consequently, appropriate values of γ_n can be determined from measured co-efficients of restitution via the relation [19]

$$e = \exp \left[- \frac{\pi}{(8K_n/(\gamma_n^2 m_p) - 1)^{1/2}} \right] \quad (4)$$

Note that this particle interaction model leads to a collision time for individual binary collisions t_c given by

$$t_c = -2 \frac{\ln(e)}{\gamma_n} \quad (5)$$

Thus, in the limit of ideally plastic collisions where $e \rightarrow 0$, the contact time $t_c \rightarrow \infty$. This model has the feature that the contact properties can be readily related to the co-efficient of restitution e as used in most analytical treatments.

Unless otherwise specified, the calculations presented below assume a particle diameter $D = 200 \mu\text{m}$ and unit out-of-plane thickness (i.e. $b = 1 \text{ mm}$). The sand particles are made from silica with a density $\rho_s = 2700 \text{ kg m}^{-3}$ while the normal stiffness is $K_n = 7300 \text{ kNm}^{-1}$. The co-efficient of restitution for impacts between the particles and between the particles and boundary wall are both taken to be $e = 0.8$ (i.e. the value of γ_n for inter-particle contacts was twice that for impacts between the particles and the walls). Following [26,27] we take $K_s/K_n = 2/7$ and the reference value of the friction co-efficient is $\mu = 0.7$. While the bulk of the calculations are presented for these reference values, we shall discuss the (usually weak) sensitivity of the results to the choice of the parameters K_n , e and μ .

The calculations were performed using the GRANULAR package in the molecular dynamics code LAMMPS. The Newton equations for both the translational and rotational motions of the particles were integrated using a Verlet time-integration scheme (i.e. Newmark-Beta with $\beta = 0.5$). The time-step was typically taken to be about $t_c/10$ in order to ensure accurate integration of the contact relations, Eqs. (1) and (2).

3. Impact of discs of sand particles against a stationary rigid target

As a first step towards understanding the interaction between deformable structures and high velocity sand sprays, we consider impact of a long column of sand particles against a stationary target as sketched in Fig. 3a. The sand impacts the target with no lateral

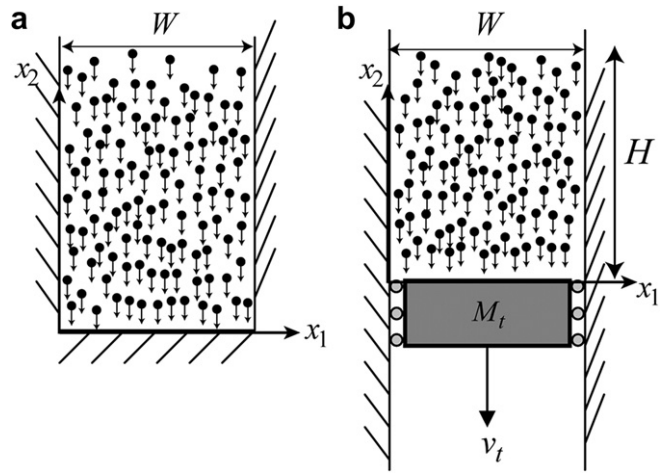


Fig. 3. Sketches of the two boundary value problems analysed. Both problems comprise a column of identical particles with relative density $\bar{\rho}$ all travelling at an initial velocity v_0 impacting (a) a rigid stationary target and (b) a rigid-freely supported target of areal mass M_t . In problem (a) the column is semi-infinite while in problem (b) the column has a finite height H .

spread: this constraint is representative of the situation near the centre of a panel loaded by a spray of sand with zero obliquity in which the sand near the periphery of the panel constrains the lateral flow of the sand near the centre of the panel.

3.1. Overview of the impact process

It is useful to first describe in broad qualitative terms the relevant phenomena that will later be illustrated via full numerical simulations. Consider the impact of a sand column comprising a loose aggregate of particles of diameter D travelling at a uniform velocity v_0 in the negative x_2 direction as shown in Fig. 4a. The aggregate has an initial relative density $\bar{\rho}$ of particles and densifies against the rigid stationary target with a densification front that advances in the positive x_2 direction, as shown in Fig. 4b. The transition from the loose to dense regions has a finite width (Fig. 4b) which depends upon the properties of the particle aggregate. Within this transition region, significant amounts of energy are dissipated via multiple collisions between the particles. When the compressive densification front reaches the distal (free) surface of the column, it reflects as a tensile wave that spalls the particles in the positive x_2 direction (Fig. 4c). This tensile wave traverses through the column and causes all the particles to be reflected back from the target (Fig. 4d). The difference between the incident and final momentum of the aggregate of particles equals momentum transmitted to the target, by momentum conservation.

Recall that the contact model between the particles is characterized by a set of particle interaction parameters (K_n, e, μ) : the ratio K_s/K_n is always held fixed and thus K_s is not an independent parameter. Then it follows from dimensional analysis that the transient pressure p exerted by the sand column on a rigid stationary structure has the functional form

$$\frac{pD}{K_n} = f \left(\bar{\rho}, \mu, e, \frac{\rho_s v_0^2 b}{K_n}, \frac{t v_0}{D}, \frac{D}{b} \right) \quad (6)$$

where t is the time measured from the instant of impact. We shall show subsequently that the steady-state pressure p_{ss} exerted by an infinitely long column on the rigid stationary structure has the form

$$\frac{p_{ss} \varepsilon D}{\bar{\rho} \rho_s v_0^2} \approx 1 \quad (7)$$

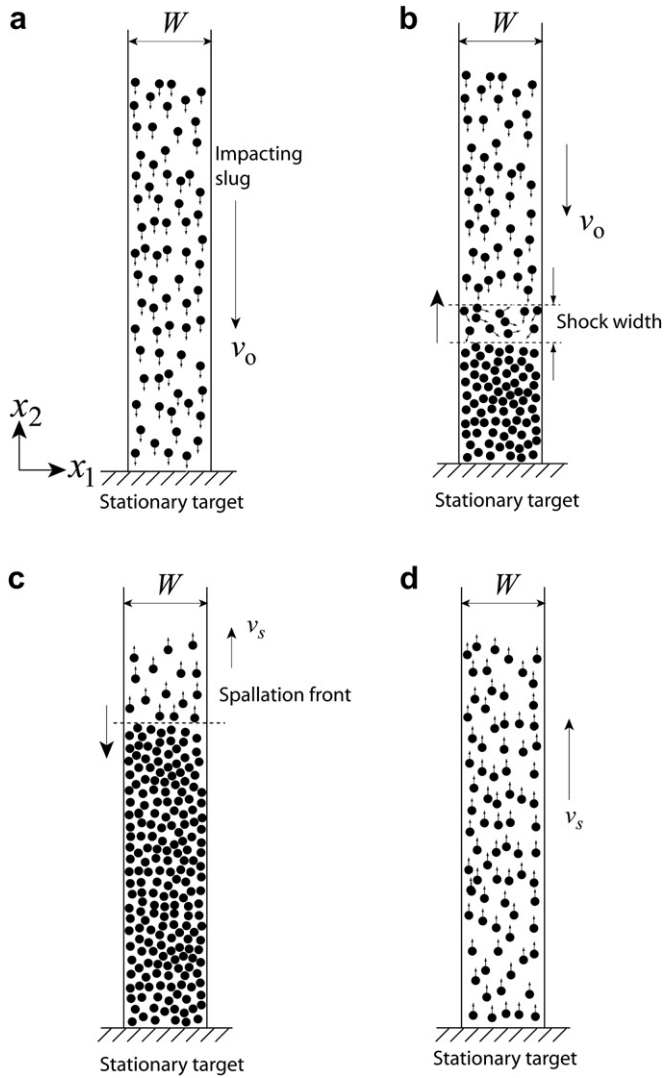


Fig. 4. Sketches of a low relative density assemblage of mono-sized particles impacting a rigid target. Lateral expansion of the assemblage is prevented by a cylindrical tube. (a) Just prior to impact; (b) The partially densified assemblage with the densification front moving in the opposite direction of the initial particle velocity. (c) The compressive densification front reflects from the free edge of the assemblage as a tensile wave causing the reflection of the particles. (d) This tensile front travels through the assemblage and reaches the target. At this point all the particles now have a velocity opposite in direction to their initial velocity. The width of the densification shock front in indicated in (b). From Deshpande et al. [19].

where ε_D is the densification strain of the compacted aggregate and is only function of $\bar{\rho}$. The steady-state shock width w has the functional form

$$\frac{w}{D} = g\left(\bar{\rho}, e, \frac{\rho_s v_o^2 b}{K_n}\right) \quad (8)$$

3.2. The boundary value problem

The two-dimensional boundary value problem under consideration is sketched in Fig. 3a. The sand column comprises a random arrangement of identical cylindrical particles of diameter D with uniform initial spatial relative density $\bar{\rho}$ and no particles that are in contact. Each particle has an initial velocity v_o in the negative x_2 direction. The column has a width $W = 500D$ and is constrained from lateral expansion by stationary rigid walls at $x_1 = (0, W)$. The column impacts a stationary rigid wall located at

$x_2 = 0$; this wall is subsequently called the target. In all calculations presented in this section, the column is sufficiently long in the x_2 direction that the densification front does not reach the end of the column over the duration of the calculation, i.e. the column may be treated as infinitely long. Time $t = 0$ is the instant at which the particles first impact the target and the nominal pressure p exerted on the target is calculated from the N particles in contact with the target as

$$p = \frac{\left| \sum_{i=1}^N F_2^i \right|}{Wb} \quad (9)$$

where F_2^i is the force exerted in the x_2 direction by the i th particle in contact with the target. We define the normalised pressure and time as

$$\bar{p} \equiv \frac{p}{\bar{\rho} \rho_s v_o^2}, \quad (10a)$$

and

$$\bar{t} \equiv \frac{tv_o}{D} \quad (10b)$$

respectively, while the normalised impact velocity is defined as

$$\bar{v}_o \equiv v_o \sqrt{\frac{\rho_s b}{K_n}}. \quad (11)$$

A snapshot from the discrete element simulation performed in LAMMPS is shown in Fig. 5a for a situation similar to that illustrated in Fig. 4b. The associated \bar{p} versus \bar{t} history for a $\bar{\rho} = 0.2$ sand column impacting at $v_o = 500 \text{ ms}^{-1}$ ($\bar{v}_o = 0.304$) is plotted in Fig. 5b. After an initial transient response where \bar{p} decreases with increasing \bar{t} , the pressure reaches a steady-state with $\bar{p} \approx 1.2$. We shall discuss the significance of this finding in Section 3.4.

3.3. The shock structure

Consider a sand column of effective relative density $\bar{\rho} = 0.2$ with an initial particle velocity $\bar{v}_o = 0.304$ in the negative x_2 direction. Contours of the component of the particle velocity $|v_2|$ in the column at three selected times are shown in Fig. 6a and b for $e = 0.5$ and $e = 0.99$, respectively (with all other parameters held fixed at their reference value). These contours are plotted by “meshing” the domain with 3-noded triangles with particles at the nodes of the triangles. Three zones are observed in both Fig. 6a and b. In the red zone I region, particles have their initial spatially uniform velocity and no information regarding the impact of the column against the target has reached the particles. The blue zone III region consists of particles that have densified against the target and exhibit only small velocities due to vibratory motions. The transition from stationary particles in zone III to particles with uniform initial velocity in zone I occurs over a transitional zone II. Within this transitional zone, large numbers of collisions are taking place and the kinetic energy lost during each collision reduces the velocity of the particles from v_o to nearly zero (with some energy being stored as elastic energy in the densified zone III). This transition zone II is referred to as the “shock”. Comparing Fig. 6a and b, it is clear that the shock width w is greater for $e = 0.99$ than for $e = 0.5$.

In order to further quantify this shock width w , we plot distributions of average particle velocity component $\langle v_2 \rangle$ as a function of co-ordinate x_2 at three selected times in Fig. 7a and b for $e = 0.99$ and $e = 0.5$ respectively. We calculate $\langle v_2 \rangle$ as follows.

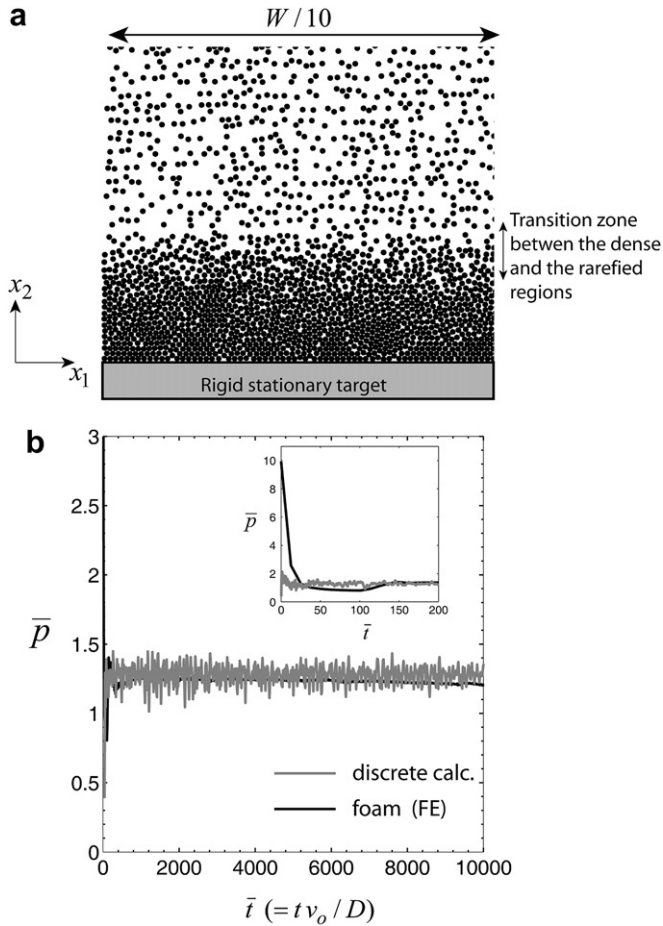


Fig. 5. (a) A snapshot from the output of the discrete calculations of the semi-infinite column ($\bar{\rho} = 0.2$, $\bar{v}_0 = 0.304$) impacting a stationary target showing a situation similar to that sketched in Fig. 4b. (b) The corresponding predictions of the normalised pressure \bar{p} versus normalised time \bar{t} history from both the discrete calculations as well as the finite element calculations using the foam model. The inset shows a magnified view of the initial portion of the \bar{p} versus \bar{t} history.

First we divide the column into horizontal strips of height $0.5D$ and width W . The average velocity $\langle v_2 \rangle$ over each strip is then calculated by averaging the velocity component v_2 of all particles in the strip. This average velocity is then plotted in Fig. 7 with x_2 taken as the mid-point of each strip. The three zones I–III are distinct in Fig. 7 with the densification front moving up the sand column (i.e. increasing x_2) with increasing time. Further, the width of the shock (zone II) over which $\langle v_2 \rangle / v_0$ transitions from -1 to approximately 0 is seen to remain approximately constant, i.e. the shock attains a steady-state width which we denote as w . The main distinction between the $e = 0.99$ and $e = 0.5$ cases is that w is higher for $e = 0.99$ compared to the $e = 0.5$ case. In order to provide a precise definition for the shock width, we arbitrarily define w as the width over which $\langle v_2 \rangle / v_0$ changes from -0.85 to -0.15 as shown in Fig. 7a.

The dependence of the normalised shock width w/D upon e , $\bar{\rho}$ and \bar{v}_0 is shown in Fig. 8a–c, respectively. The main finding is that w decreases with decreasing e (as the collisions between the particles become more plastic). In fact w becomes on the order of a single particle diameter for $e \leq 0.5$. The shock also sharpens (w decreases) with increasing $\bar{\rho}$ and \bar{v}_0 and approaches a few particle diameters at high impact velocities. The implications of these findings for an effective constitutive relation of the aggregate of particles are discussed in Section 3.5.

3.4. Effect of column properties on the pressure exerted by the column

The pressure \bar{p} versus \bar{t} history shown in Fig. 5b suggests that the pressure exerted by the sand column on the target reaches a steady-state value at $\bar{t} \geq 2000$. We define the steady-state pressure \bar{p}_{ss} as the average pressure over the interval $2000 \leq \bar{t} \leq 4000$. Bearing in mind the scaling in Eq. (7), the dependence of $\bar{p}_{ss}\epsilon_D$ upon $\bar{\rho}$ and e is given in Fig. 9a and b, respectively, for two choices of the impact velocity \bar{v}_0 . (Recall that ϵ_D is the densification strain of the loose aggregate.) The numerical calculations suggest that the aggregate densifies to a maximum relative density $\bar{\rho}_{max} = 0.9$ and hence in Fig. 9a and b we employ ϵ_D as given by

$$\epsilon_D = 1 - \frac{\bar{\rho}}{\bar{\rho}_{max}} \quad (12)$$

The numerical results illustrate that $\bar{p}_{ss}\epsilon_D$ decreases slightly with increasing \bar{v}_0 and $\bar{\rho}$. The mild dependence of $\bar{p}_{ss}\epsilon_D$ upon $\bar{\rho}$ and \bar{v}_0 is due to the finite elasticity of the densified aggregate and will be explained via an analytical model in Section 3.5. The numerical results in Fig. 9b clearly show that e has a negligible effect upon the pressure exerted by the column on the target. There is a similarly negligible (not shown) effect of friction μ up on \bar{p}_{ss} . We conclude that the loading due to the sand column upon the target is mainly inertial in nature and scales with $\bar{\rho}\rho_s v_0^2 / \epsilon_D$. The normal contact stiffness K_n affects the elasticity of the densified aggregate and has a small effect on the pressure as shown below. Otherwise, the contact properties of the particles have minimal effect on the pressure exerted on a target.

3.5. The foam analogy

The sketch of the impact process prior to the onset of spallation (Fig. 4) is reminiscent of a foam impacting a rigid stationary target. This motivates us to develop an analogy between the impact of a rigid wall by a constrained sand column and by a foam projectile.

Consider a foam projectile of density ρ_m and quasi-static uniaxial compressive response, as sketched in Fig. 10a. The foam is assumed to have zero strength and compresses at zero stress up to its nominal densification strain ϵ_D whereupon the stress increases linearly with increasing compressive strain with a tangent modulus E . We emphasize here that while the particles in the discrete calculation undergo recoverable elastic compression beyond the densification strain ϵ_D , in the analytical solution presented subsequently the entire deformation of the foam including beyond ϵ_D is plastic and irrecoverable. A projectile made from this foam travelling at an initial velocity v_0 impacts a rigid stationary target at time $t = 0$. We develop an analysis for the pressure p exerted by the foam on the target by modifying the analyses of Reid and co-workers [28,29] and Deshpande and Fleck [30]. After the impact, a plastic shock wave is initiated in the projectile at the interface between the projectile and target and travels through the projectile at a Lagrangian speed c_{pl} as illustrated in Fig. 10b. Because the projectile had a zero compressive strength, the stress immediately ahead of the shock is zero. The material behind the shock has the velocity of the target, i.e. $v_t = 0$ and a uniaxial stress p associated with a compressive strain ϵ_L . In contrast, the material ahead of the shock is undeformed and travelling at the initial velocity v_0 . Mass and momentum conservation across the shock front dictate

$$c_{pl} = \frac{v_0}{\epsilon_L} \quad (13a)$$

and

$$p = \rho_m c_{pl} v_0 \quad (13b)$$

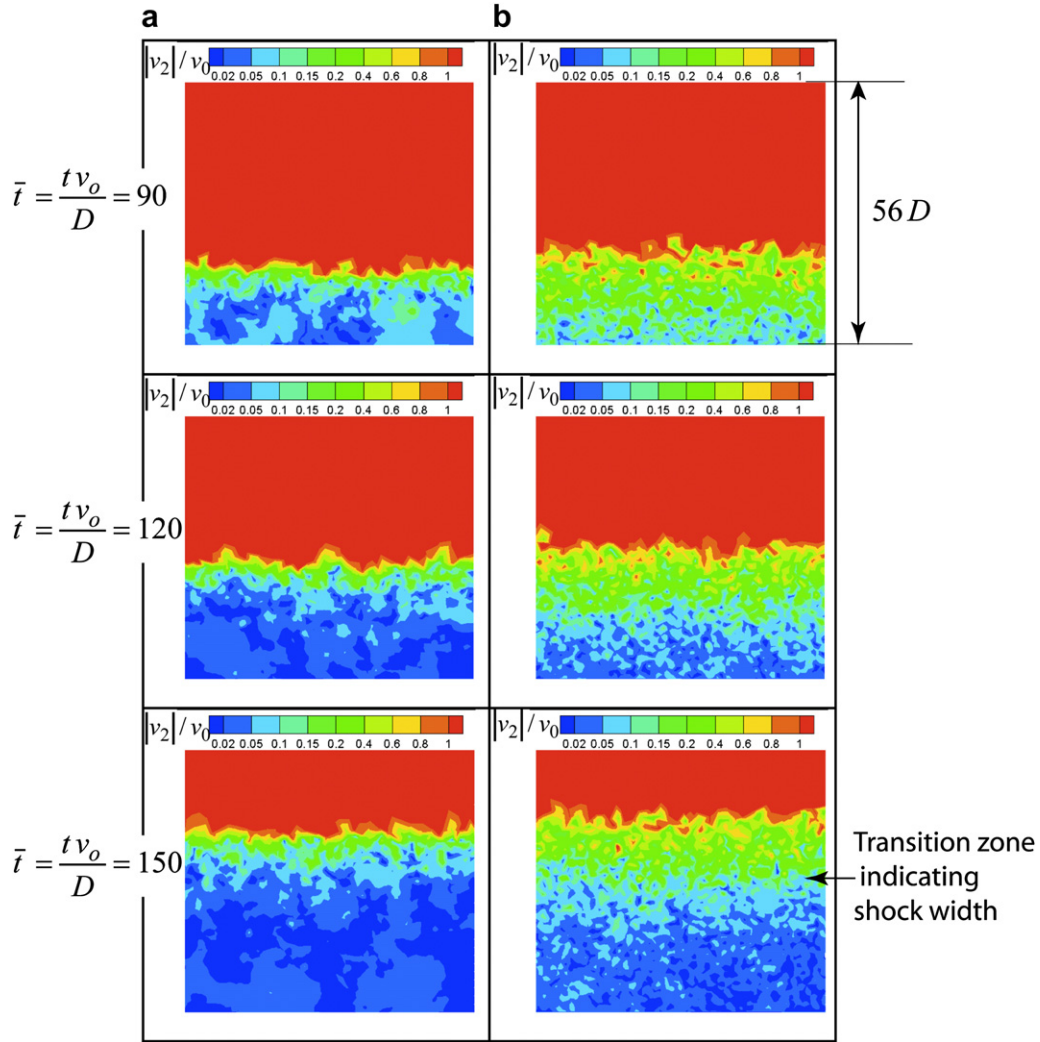


Fig. 6. Snapshots from the discrete calculations showing the distributions of the normalised velocity $|v_2|/v_0$ at three selected times \bar{t} after impact of the $\bar{p} = 0.2$ and $\bar{v}_o = 0.304$ semi-infinite column against a stationary target. The co-efficient of restitution between particles is (a) $e = 0.5$ and (b) $e = 0.99$.

respectively. Given that the stress in the densified portion of the projectile is p , it follows from the constitutive relation sketched in Fig. 10a that the lock-up strain is

$$\epsilon_L = \epsilon_D + \frac{p}{E} \quad (14)$$

Combining Eqs. (13) and (14) it follows that the pressure p is given by

$$\bar{p}\epsilon_D = \frac{p\epsilon_D}{\rho_m v_o^2} = \frac{E\epsilon_D^2}{2\rho_m v_o^2} \left[\sqrt{1 + \frac{4\rho_m v_o^2}{E\epsilon_D^2}} - 1 \right], \quad (15)$$

which corresponds to the Rayleigh line sketched in Fig. 10a. Thus, a constant pressure \bar{p} is exerted on the target and this pressure should be interpreted as the steady-state pressure \bar{p}_{ss} .

In order to complete the analogy and make quantitative comparisons we need to specify the parameters ρ_m , ϵ_D and E and take v_o to be identical for the sand column and foam projectile. The density of the foam projectile is taken to be equal to that of the sand column, i.e. $\rho_m = \bar{p}\rho_s$, with ϵ_D for the foam projectile given by Eq. (12) in order to be consistent with the discrete calculations. It now remains to specify the modulus E of the projectile beyond the densification strain ϵ_D . In order to make a direct connection with

the elasticity of the densified aggregate we calculate E by analyzing a close packed array of discs as sketched in Fig. 11. This arrangement has a maximum relative density $\bar{\rho}_{max} = \pi/(2\sqrt{3}) \approx 0.9$ and is representative of the aggregate in the densified state as given by the discrete model calculations. The discs in the close packed lattice (Fig. 11) have a normal contact stiffness K_n . A simple modification of the analysis for a triangulated lattice by Gibson and Ashby [31] gives the relation between E (which is the modulus under uniaxial straining) and K_n as

$$E = \frac{3\sqrt{3}K_n}{4b} \quad (16)$$

Thus, there is direct connection between the properties of the foam and the sand column with no additional parameters in the foam model that require fitting or calibration. Combining Eqs. (15) and (16) gives an expression for \bar{p} in terms of the parameters in the discrete model as

$$\bar{p}\epsilon_D = \frac{\epsilon_D^2}{\sqrt{3}\bar{\rho}_o^2} \left(\frac{D}{b} \right) \left[\sqrt{1 + \frac{2\sqrt{3}\bar{p}v_o^2}{\epsilon_D^2} \left(\frac{D}{b} \right)} - 1 \right] \quad (17)$$

where ϵ_D is given by Eq. (12). We now proceed to compare the analytical predictions of the “foam” model with the discrete

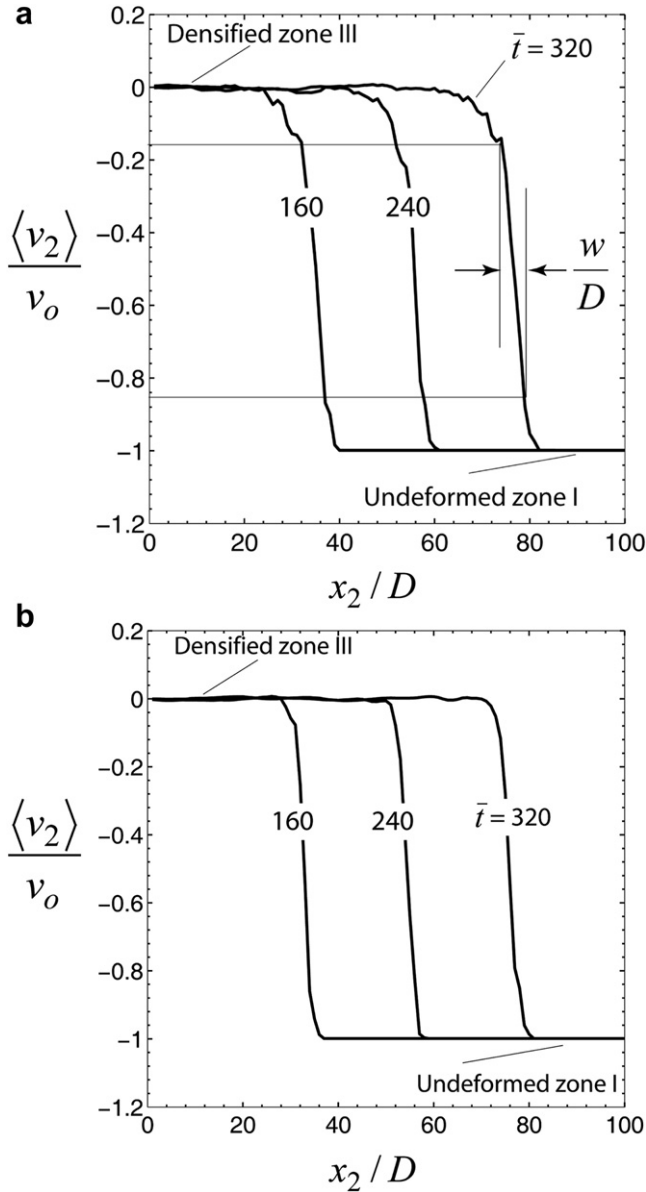


Fig. 7. Plots showing the averaged velocity $\langle v_2 \rangle$ as a function of the position x_2 at three selected times after the impact for a $\bar{\rho} = 0.2$ and $\bar{v}_o = 0.304$ semi-infinite column against a stationary target. The co-efficient of restitution between particles (a) $e = 0.99$ and (b) $e = 0.5$.

calculations as presented above and also with finite element (FE) calculations of foam projectile impact. Details of these FE calculations, including the constitutive model employed in the FE calculations, are given in Appendix A.

The FE predictions of $\bar{\rho}$ versus \bar{t} for the $\bar{\rho} = 0.2$ equivalent foam impacting at $\bar{v}_o = 0.304$ are included in Fig. 5b. The FE calculations predict an initial peak followed by a transient response during which $\bar{\rho}$ decreases with increasing \bar{t} . Subsequently, the pressure settles to a steady-state that is in excellent agreement with the discrete calculations. The analytical solution only gives the steady-state solution and it agrees well with both the FE and discrete calculations; recall Fig. 9a. The initial transient response in the FE calculations is a result of the viscosity in the constitutive model used in the FE calculations (see Appendix A for a discussion on this topic). This transient typically has a higher peak than that

observed in the discrete calculations. Comparisons between the discrete and continuum foam (analytical and FE) predictions of $\bar{\rho}_{ss} \varepsilon_D$ as a function of $\bar{\rho}$ for the two selected values of \bar{v}_o are included in Fig. 9a. The analytical and FE predictions for the foam model agree extremely well with each other and with the discrete predictions (to within 5%).

It is worth emphasizing the differences between the FE and analytical calculations using the foam model. The principle difference lies in the fact that the analytical model assumes a sharp shock, i.e. discontinuity in the velocity field while the viscosity within the constitutive model implies that there is no discontinuity in the FE calculations. Rather, the FE calculations predict a shock of finite width (similar to the discrete calculations). The shock width for an assumed linear viscosity qualitatively predicts the features seen in Fig. 8b and c, viz. that the shock width decreases with increasing impact velocity and initial projectile density. Note that the structure of the shock does not affect the steady-state pressure exerted on the target and so we do not attempt to emulate the shock structure as observed in the discrete calculations. As done in Radford et al. [33], we employ viscosity as a numerical tool in the FE calculations in order to resolve the shock in a Lagrangian FE setting.

4. Interaction of sand columns with rigid movable targets

We proceed to analyse the one-dimensional “soil-structure” interaction problem as sketched in Fig. 3b. Here a constrained sand column of height H comprising an aggregate of discs travelling at a spatially uniform velocity v_o in the negative x_2 direction impacts a rigid unsupported target of areal mass M_t at time $t = 0$. The sand slug has an initial relative density $\bar{\rho}$. The target is constrained to move in the x_2 direction and the column is constrained against lateral expansion as illustrated in Fig. 3b. Both discrete and continuum foam calculations of the problems are presented in this section. The discrete calculations were carried out in a similar manner to that described in Section 3 except that there now exists an additional linear equation of motion for the target in the x_2 direction. Furthermore, the sand column now has a finite height H and has a finite areal mass $M_s = \bar{\rho} \rho_s H$. The calculations are carried out until both the target and sand particles acquire a steady-state velocity. This steady-state is achieved soon after the densification front reaches the top, free surface of the column and reflects as a spallation front (recall that in Section 3, the calculations related to an infinitely long column and hence no spallation occurred).

The sand column has an initial incoming momentum per unit area $I_o = M_s v_o$ and the main aim is to determine the areal momentum I_t transmitted into the target. Extending the dimensional analysis of Section 3, gives

$$\frac{I_t}{I_o} = f\left(\bar{\rho}, \mu, e, \bar{v}_o, \hat{t}, \bar{M}, \frac{D}{b}\right) \quad (18)$$

where

$$\hat{t} \equiv \frac{t v_o}{H} \quad (19a)$$

and

$$\bar{M} \equiv \frac{M_t}{M_s} \quad (19b)$$

Unless otherwise specified, all calculations presented here were performed for a sand column of areal mass $\bar{\rho} \rho_s H = 135 \text{ kg m}^{-2}$ with an initial velocity $v_o = 500 \text{ ms}^{-1}$ (i.e. $\bar{v}_o = 0.304$).

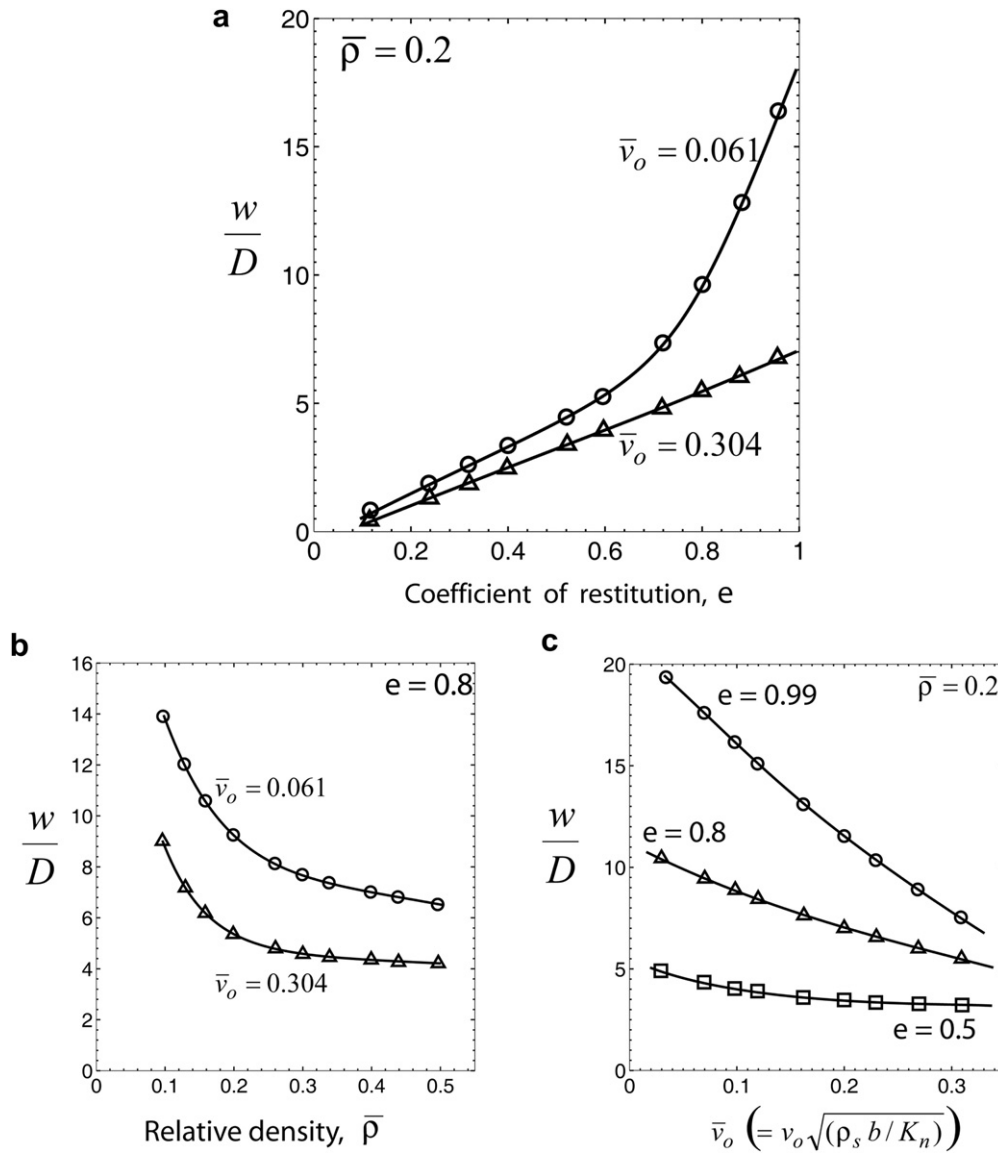


Fig. 8. The dependence of the normalised steady-state shock width w/D on (a) co-efficient of restitution e , (b) relative density $\bar{\rho}$ and (c) normalised velocity \bar{v}_o . The parameters held fixed are indicated in each of the figures.

4.1. Analysis of the two reference cases

Snapshots showing the position of the sand particles and target at selected times after impact by a $\bar{\rho} = 0.2$ sand column with an initial velocity $\bar{v}_o = 0.304$, are shown in Fig. 12a and b for $\bar{M} = 1$ and $\bar{M} = 16$, respectively. First consider the case of a light target with $\bar{M} = 1$. After impact, the column progressively densifies against the target, and the target accelerates. The densification front reaches the top or free surface of the column and reflects as a spallation wave. Given that the target has an identical mass to the column, the target acquires a final velocity of approximately $0.5v_o$ suggesting a near plastic collision between the sand slug and the target. The densification or shock front is relatively weak and minimal spallation occurs in this case. In contrast, in the $\bar{M} = 16$ case, the heavy target acquires a velocity that is a small fraction of v_o . The resultant strong shock gives rise to significant spallation as it reflects from the top surface of the sand column.

The normalised momentum acquired by the target $\bar{I}_t = I_t/I_o$ is plotted in Fig. 13a as a function of the normalised time \hat{t} . In these

figures both the $\bar{M} = 1$ and $\bar{M} = 16$ cases are included along with the reference case of a stationary target which corresponds to $\bar{M} \rightarrow \infty$. The target acquires its steady-state velocity shortly after the densification front reaches the top or free end of the column. We label this time as t_{ss} and the corresponding momentum of the target as I_t^{ss} . The steady-state momentum I_t^{ss} acquired by the target increases with increasing \bar{M} and exceeds the incoming momentum I_o for $\bar{M} = 16$ and $\bar{M} \rightarrow \infty$ (the stationary target). This arises because spallation results in reflection (or bounce) of the entire sand column from the target. Momentum conservation then implies that the target acquires a momentum greater than I_o . In contrast, the momentum acquired by a light target of normalised mass $\bar{M} = 1$ is less than I_o because a significant fraction of the sand column continues to move in the direction of the target. We will revisit this issue of sand rebound in Section 4.2.

The normalised pressure \bar{p} exerted by the sand on the target is plotted in Fig. 13b corresponding to the target momentum results in Fig. 13a. This interface pressure $\bar{p} \approx 1.5$ for all three values of \bar{M} at

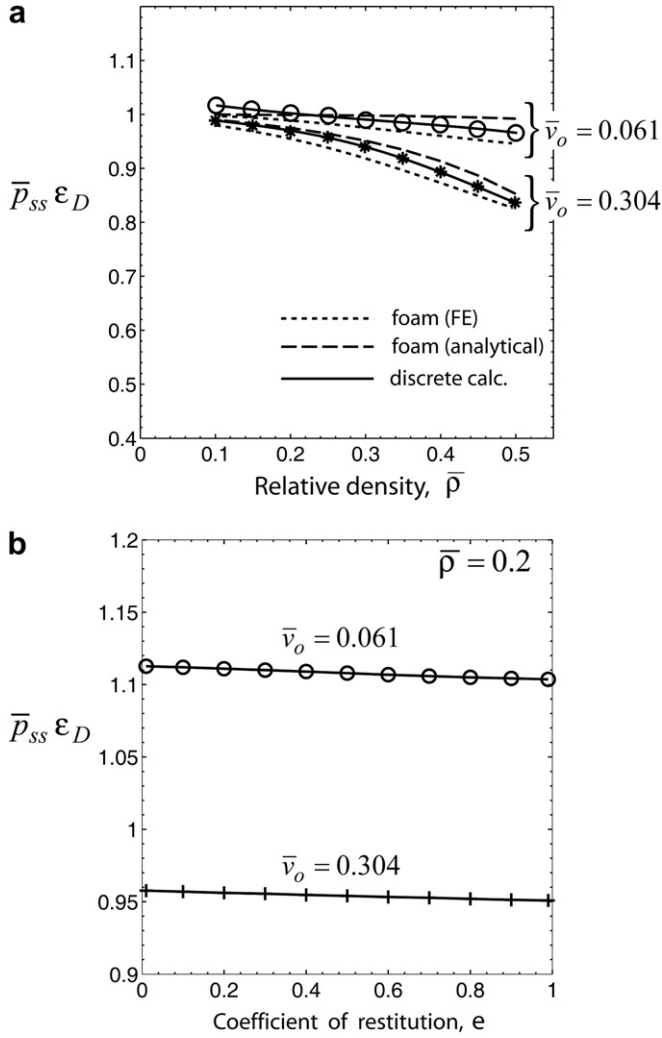


Fig. 9. Dependence of the normalised steady-state pressure $\bar{P}_{ss} \epsilon_D$ on (a) relative density $\bar{\rho}$ and (b) co-efficient of restitution e for the impact of a semi-infinite column against a stationary target. The parameters held fixed are indicated in each of the figures.

$\hat{t} = 0$. Subsequently, the pressure remains approximately constant for the case of the stationary target ($\bar{M} \rightarrow \infty$) but decreases with increasing \hat{t} as the velocity difference between the incoming sand particles and the target decreases. This is often referred to as the “soft catch” mechanism that reduces momentum transfer to the target.

4.2. The steady-state momentum transfer to target

Predictions of the steady-state momentum acquired by the target I_t^{ss} are plotted in Fig. 14a as a function of the mass ratio \bar{M} for three choices of the initial relative density $\bar{\rho}$ of the sand column. The momentum acquired by the target increases not only with increasing \bar{M} but also with increasing $\bar{\rho}$. The increase in I_t^{ss} with \bar{M} and $\bar{\rho}$ is due to the increase in rebound of the sand from the target: with both increasing \bar{M} and $\bar{\rho}$ the pressure exerted on the target increases which results in a larger elastic compression of the densified aggregate and the subsequent rebound results in a larger momentum transfer to the target.

Recall that the co-efficient of restitution between the particles and between the particles and the target is $e = 0.8$. Thus for a single particle impacting the target, the momentum acquired by the target would be given by

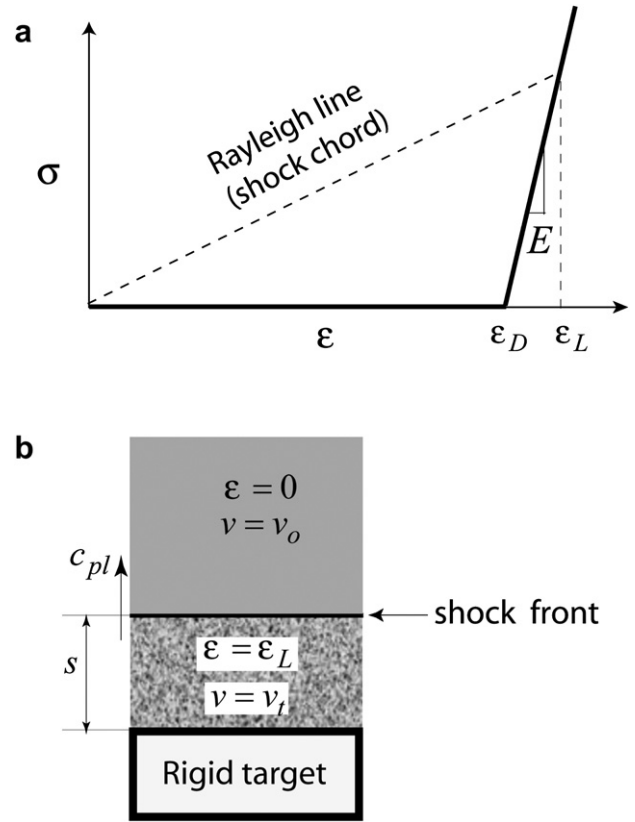


Fig. 10. (a) The idealised quasi-static uniaxial straining compressive response of a sand column with a low relative density of particles and (b) schematic of the impact process of a foam against a target of areal mass M_t .

$$\bar{I}_t^{ss} = \frac{\bar{M}}{1 + \bar{M}}(1 + e) \tag{20}$$

However, the results in Fig. 14a indicate that the multiple collisions between the particles and between the particles and the walls that take place during the impact of the column against the target result in an effective co-efficient of restitution e_{eff} that is significantly lower than e and dependent upon $\bar{\rho}$. By fitting Eq. (20) (with e replaced by e_{eff}) to the data in Fig. 14a we observe that the effective co-efficient of restitution between the sand and the target varies between 0 and 0.35 for the range of $\bar{\rho}$ values considered here. The predictions of the steady-state momentum \bar{I}_t^{ss} transferred into a stationary target are summarised in Fig. 15b as a function of $\bar{\rho}$: \bar{I}_t^{ss} rises to about 1.35 for $\bar{\rho} = 0.5$, i.e. the maximum value of e_{eff} is 0.35. We conclude that the momentum transferred to a stationary target can be about 35% greater than

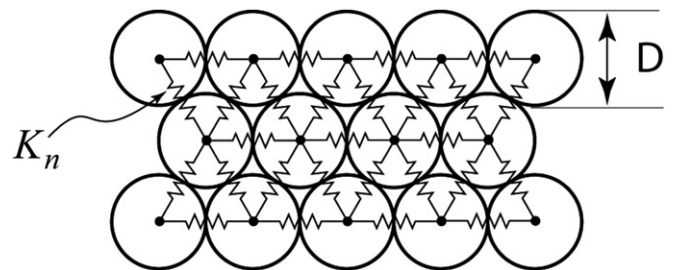


Fig. 11. Sketch of the fully dense aggregate of the identical discs of diameter D with an inter-particle contact stiffness K_n .

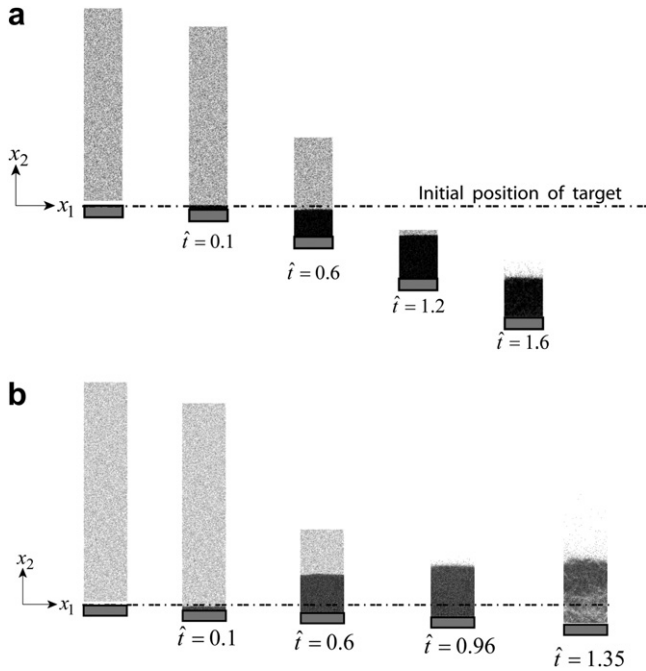


Fig. 12. Snapshots from the discrete calculations showing the positions of the particles and target at selected times after the impact of the $\bar{\rho} = 0.2$ and $\bar{v}_o = 0.304$ slug. The mass ratio of the target to column is (a) $\bar{M} = 1$ and (b) $\bar{M} = 16$.

the incoming momentum of the sand due to rebound of the sand from the target.

In order to clarify the effect of bounce-back, we plot in Fig. 15 the momentum acquired by the target I_t^{ss} as well as the steady-state momentum I_R^{ss} of the sand particles that are continuing to move in the direction of motion of the target. We shall subsequently refer to this momentum I_R^{ss} as the residual momentum of the sand particles. The momentum of the sand particles that have bounced back and are now travelling in the opposite direction to the target is then given as $I_b^{ss} = (I_t^{ss} + I_R^{ss}) - I_o$. The results in Fig. 15 are plotted as function of \bar{M} for a sand column of relative density $\bar{\rho} = 0.2$. Two important features are noted from this figure:

- (i) The low momentum transfer to the target at small values of \bar{M} arises because there is no bounce-back of the sand; most of the sand continues to travel with the target so that $I_t^{ss} + I_R^{ss} \approx I_o$.
- (ii) At high values of \bar{M} , $I_R^{ss} \approx 0$ but $I_t^{ss} > I_o$ as all the particles bounce back and travel in the direction opposite to their initial velocity.

The normalised time \hat{t}_{ss} required for the target to attain its steady-state velocity is plotted as a function of the mass ratio \bar{M} in Fig. 16 for three choices of $\bar{\rho}$. This can be thought of as the “fluid-structure” interaction time of the sand and the target in this one-dimensional setting. The dependencies on \bar{M} and $\bar{\rho}$ seen in Fig. 16 will be rationalised in the context of the foam analogue in Section 4.4.

4.3. Effect of sand properties on the momentum transfer

Eq. (18) suggests that in addition to \bar{M} and $\bar{\rho}$, $\bar{I}_t^{ss} \equiv I_t^{ss}/I_o$ may also have a functional dependence on $(e, \mu, D/b$ and $\bar{v}_o)$. The dependence of \bar{I}_t^{ss} on \bar{v}_o is shown in Fig. 17a and b for selected values of \bar{M} for $\bar{\rho} = 0.1$ and $\bar{\rho} = 0.4$, respectively. There is negligible dependence upon \bar{v}_o in the $\bar{\rho} = 0.1$ case over the entire range of \bar{M} values

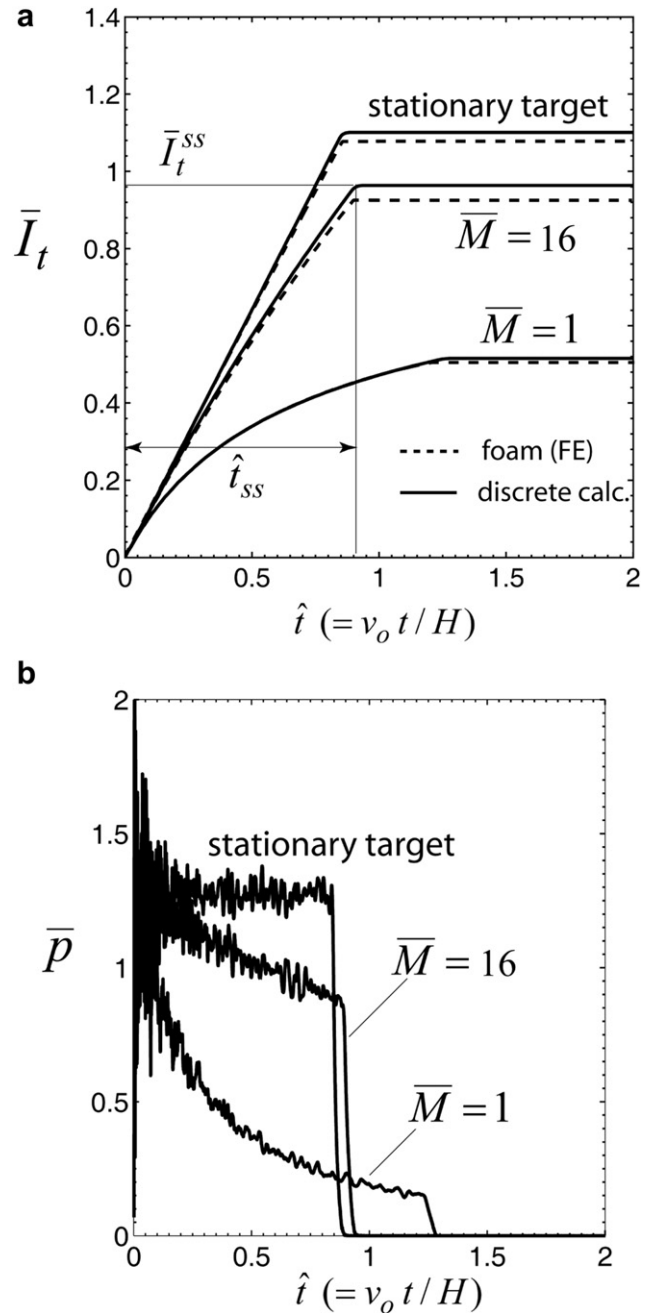


Fig. 13. (a) The temporal variation of the normalised momentum \bar{I}_t transferred to the target for impact of the $\bar{\rho} = 0.2$ and $\bar{v}_o = 0.304$ slug. (b) The corresponding normalised pressure \bar{p} exerted by the slug on the target. Results are shown for three selected values of the mass ratio \bar{M} including the stationary target corresponding to $\bar{M} \rightarrow \infty$.

but \bar{I}_t^{ss} increases slightly with increasing \bar{v}_o for the $\bar{\rho} = 0.4$ case especially when $\bar{M} \geq 8$. This is explained as follows. An increase in \bar{v}_o leads to a higher contact pressure between the column and target, and thereby to an increased elastic compression of the densified aggregate. This results in a higher transmitted momentum due to the subsequent bounce-back of the sand particles. We note in passing that the small dependence upon \bar{v}_o as indicated in Fig. 17, implies that the contact stiffness K_n between the particles also has a rather small influence on the momentum transfer to the target.

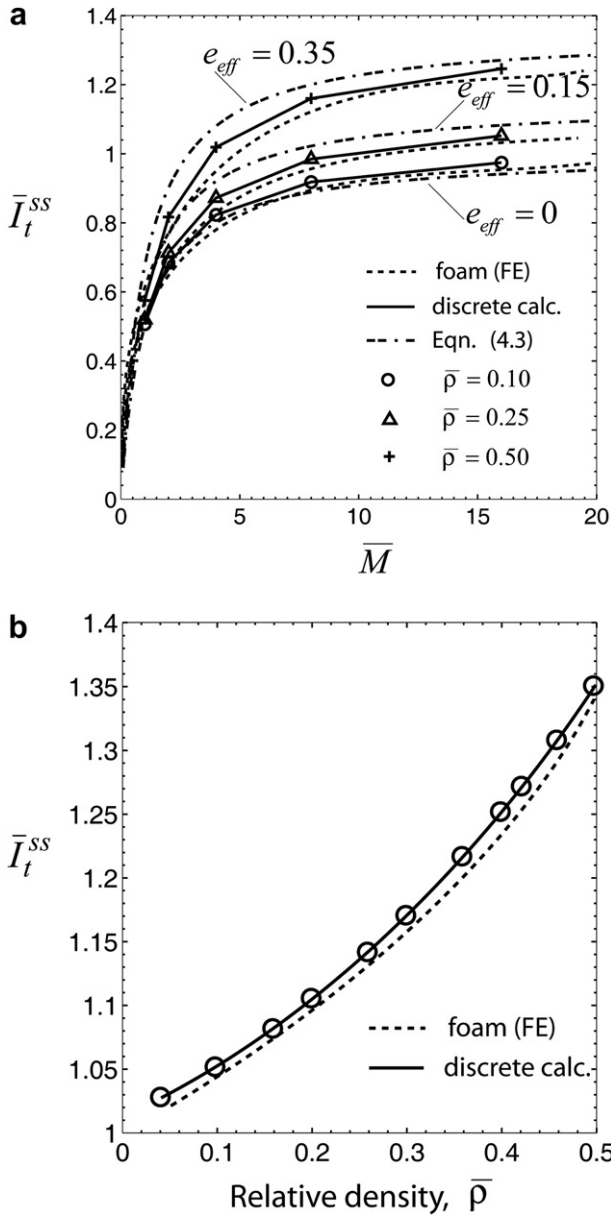


Fig. 14. (a) Predictions of the normalised steady-state momentum \bar{I}_t^{SS} transferred to the target as a function of the target to sand column mass ratio \bar{M} . Results are included for three relative density values for the column travelling at $\bar{v}_0 = 0.304$. (b) Predictions of \bar{I}_t^{SS} in the limit $\bar{M} \rightarrow \infty$ (i.e. stationary target) as a function of the column relative density $\bar{\rho}$. Predictions of the foam model are included in all cases along with a fit of Eq. (20) in (a).

For the sake of brevity we do not include results for the dependence of \bar{I}_t^{SS}/I_0 on e , μ and D/b . Numerical experimentation reveals that these parameters have a negligible (less than 1%) effect on \bar{I}_t^{SS} for all values of \bar{M} , $\bar{\rho}$ and \bar{v}_0 investigated above.

4.4. The foam analogue

We have demonstrated that sand impact against a stationary target can be represented by foam impact: the pressure exerted on the target adequately predicted by a simple foam model. We shall extend this analogue to the case of the sand column impacting a movable target. A simple analytical solution is no longer available for this case and hence we only present the FE solutions using the foam model as described in Appendix A.

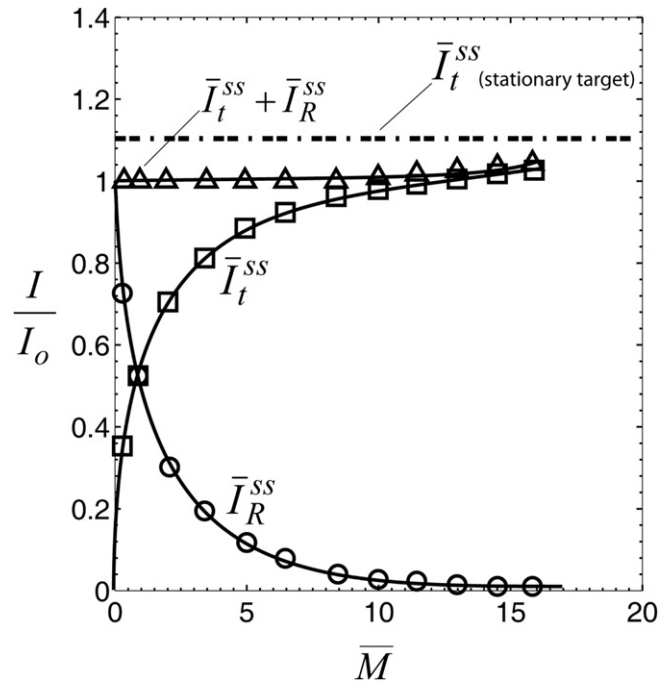


Fig. 15. Steady-state predictions of the dependence of the momentum transferred to the target \bar{I}_t^{SS} and the residual momentum in the column \bar{I}_R^{SS} in the direction of motion of the target as a function of the mass ratio \bar{M} . Results are for the $\bar{\rho} = 0.2$ and $\bar{v}_0 = 0.304$ column. The asymptote of \bar{I}_t^{SS} for the stationary target ($\bar{M} \rightarrow \infty$) is included.

Predictions of the foam model are included in Figs. 13a, 14, 16 and 17. The foam model mimics the discrete calculations with remarkable accuracy over this wide range of parameters including \bar{M} , $\bar{\rho}$ and \bar{v}_0 . Also note that the foam model does not include parameters analogous to e , μ and D/b . Recall that the level of momentum transfer in the discrete calculations is also insensitive to these parameters.

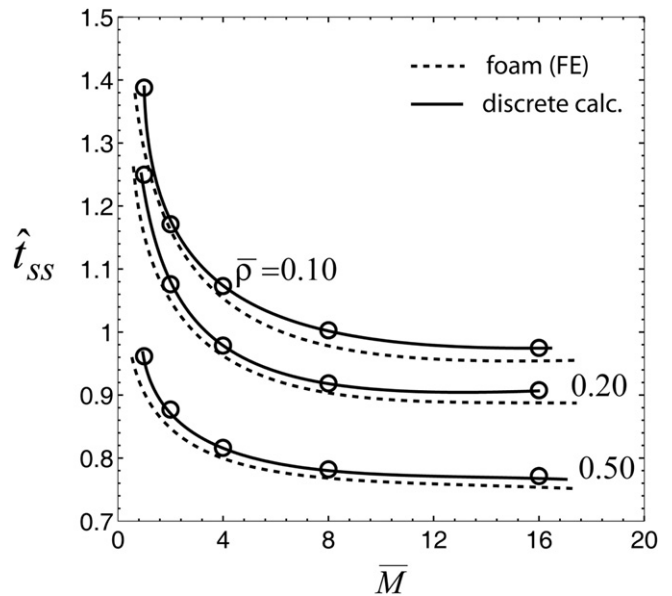


Fig. 16. Predictions of the normalised time \hat{t}_{SS} for the target to achieve its steady-state velocity when impacted by a sand column travelling at $\bar{v}_0 = 0.304$ for three selected values of the column relative density $\bar{\rho}$. Finite element predictions employing the foam model are included.

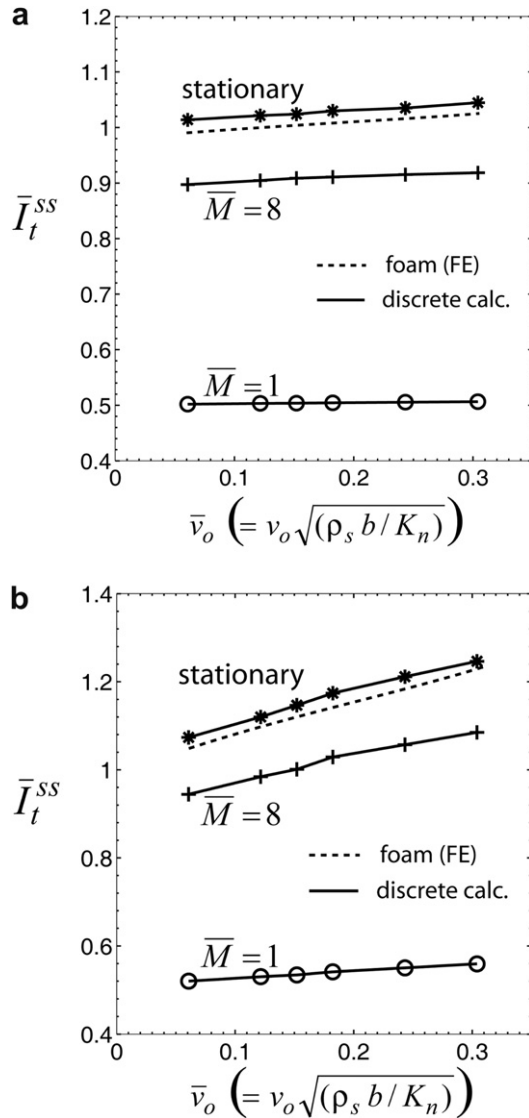


Fig. 17. The dependence of the normalised steady-state momentum \bar{I}_t^{SS} transferred to a target as a function of the normalised sand column velocity \bar{v}_o for columns with relative density (a) $\bar{\rho} = 0.1$ and (b) $\bar{\rho} = 0.4$. In each case we include results for three values of the target to sand column mass ratio including the stationary target corresponding to $\bar{M} \rightarrow \infty$.

It is worth emphasising here that the foam model does not include the spallation effects that are seen for the impacts against the heavier targets; see Fig. 12b. However, the foam model does include elasticity within the foam. This results in the rebound or bounce-back of the foam projectile. While this rebound is not precisely the same as spallation it has the same net effect in that additional momentum is transmitted into the target and resulting in the excellent agreement between the discrete and foam model predictions of the transmitted momentum seen in Fig. 13a.

Although there is no analytical solution to the situation of a foam impacting the movable target, the foam model reduces to the simple situation of a “plastic collision” in the limit $E \rightarrow \infty$. We shall pursue this model in order to understand the dependence of \hat{t}_{ss} on \bar{M} and $\bar{\rho}$ as shown in Fig. 16. Consider the situation sketched in Fig. 10b where a foam projectile of density $\bar{\rho}\rho_s$ and height H , travelling at a velocity v_o , impacts the target of mass M_t . After impact at time $t = 0$, a plastic shock wave is

initiated in the foam at the interface between the projectile and target and travels through the foam at a Lagrangian speed c_{pl} . At time t it has travelled a distance s into the foam as measured in the undeformed configuration. Since the foam has a zero compressive strength, the stress immediately ahead of the shock is zero. The material behind the shock is rigid, compressed to a strain $\varepsilon_L = \varepsilon_D$ and travels at the velocity v_t of the target. Following the analysis of Section 3.5, the governing differential equations for the motion are

$$\dot{v}_t = \frac{\sigma_D}{M_t + \bar{\rho}\rho_s s} \quad (21a)$$

$$\dot{s} = c_{pl} = \frac{v_o - v_t}{\varepsilon_D} \quad (21b)$$

and

$$\sigma_D = \bar{\rho}\rho_s c_{pl}(v_o - v_t) \quad (21c)$$

where σ_D is the stress immediately behind the shock front in the foam. This set of ordinary differential equations can be solved analytically with initial conditions $v_t = s = 0$ at $t = 0$. The steady-state solution is achieved when the shock reaches the free surface, i.e. $s = H$ and the entire foam projectile and target have a common velocity. This gives

$$\bar{I}_t^{SS} = \frac{\bar{M}}{1 + \bar{M}} \quad (22)$$

and

$$\hat{t}_{ss} = \varepsilon_D \left(1 + \frac{1}{2\bar{M}} \right) \quad (23)$$

It is evident that the dependence of \bar{I}_t^{SS} on \bar{M} is primarily due to the momentum sharing that takes place in a plastic collision. However, this model with $E \rightarrow \infty$ does not predict any dependence of \bar{I}_t^{SS} upon $\bar{\rho}$ as it does not account for the elastic deformation and subsequent spring-back of the densified aggregate. However, \hat{t}_{ss} as predicted by Eq. (23) is largely consistent with the discrete predictions in Fig. 16 including the effect of $\bar{\rho}$ that arises through $\varepsilon_D(\bar{\rho})$ from Eq. (12). The analytical model demonstrates that a reduction in clearly $\bar{\rho}$ leads to a larger densification strain and increases the time \hat{t}_{ss} for the shock front to reach the end of the sand column, for a given value of v_o . Similarly, the shock speed increases with increasing \bar{M} , and thus \hat{t}_{ss} decreases with increases values of \bar{M} .

5. Effect of constraint

All the calculations presented up to this point were for the sand column whose lateral expansion was constrained. This constraint is thought to be representative near the centre of a panel loaded by a spray of sand (Fig. 1): the sand near the periphery of the panel constrains against lateral flow of the sand near the centre of the panel. In order to investigate the range of validity of this constrained solution we now report a limited set of calculations for a sand column of height H and width W impacting a rigid stationary target as shown in Fig. 3a but with the sand column now free to expand laterally. The stationary target is sufficiently wide that it can be treated as a rigid stationary half-space in the region $x_2 < 0$, i.e. this target will not permit any particles to pass the boundary $x_2 = 0$. Unless otherwise specified, the particle contact properties are fixed at the reference values of Section 2. The key parameter that governs the effect of the lateral spreading is the aspect ratio H/W . In the limit $H/W \rightarrow 0$ we expect to recover the constrained limit while for $H/W \gg 1$ we expect to reach another asymptote corresponding to the

unconstrained limit. In all of the calculations the column dimensions were chosen so that both H/D and W/D exceed 500 so that the calculations correspond to a “continuum” limit where particle size does not play a role. All calculations presented here are for a sand column of relative density $\bar{\rho} = 0.4$ and travelling at $\bar{v}_0 = 0.304$.

Time snapshots showing the impact event of the $H/W = 4$ column against a rigid stationary target are given in Fig. 18. The snapshots show the lateral spreading of the column. They also show that a “hill” of densified particles is formed with the additional incoming particles flowing down this hill. This deformation mode is markedly different from that of the constrained column. Nearly all particles acquire a final horizontal velocity with no bounce-back as seen for the constrained case. We thus anticipate this column to transmit a smaller momentum to the target compared to its constrained counterpart. Predictions of the normalised momentum I_t/I_0 transmitted to the stationary target versus the normalised time \hat{t} are plotted in Fig. 19a for three choices of the ratio H/W including

the constrained limit corresponding to $H/W \rightarrow 0$. Both the initial rate of momentum transfer and the final value of transmitted momentum \bar{I}_t^{ss} , increase with decreasing H/W . For the $H/W = 4$ case, all particles spread laterally implying that the transmitted momentum is equal to I_0 giving $\bar{I}_t^{ss} \approx 1$. Rebound of the sand increases with decreasing H/W ; thereby the transmitted momentum increases until $\bar{I}_t^{ss} \approx 1.2$ for the fully constrained case.

Predictions of the variation of \bar{I}_t^{ss} with H/W are summarised in Fig. 19b for two choices of the friction co-efficient μ . The two asymptotes corresponding to the fully constrained case when $H/W \rightarrow 0$, and the unconstrained case when $H/W \rightarrow \infty$, are unaffected by μ . However, in the intermediate regime the results display a sensitivity to μ : the value of H/W below which the column behaviour transitions from the unconstrained to the constrained case decreases with decreasing μ . This dependence on μ is anticipated from the snapshots in Fig. 18: the angle of repose of the hill of densified particles increases with increasing μ .

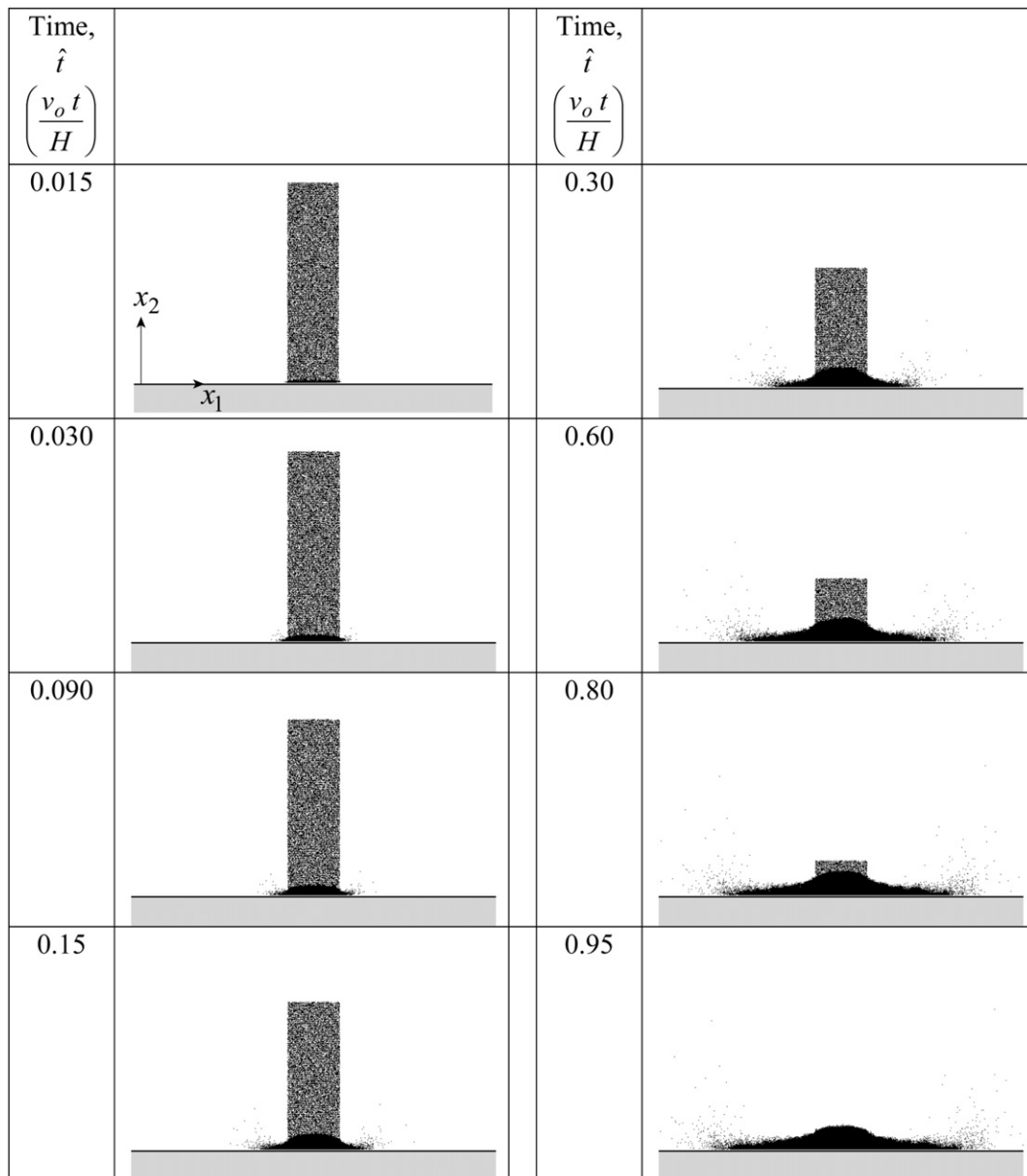


Fig. 18. Snapshots from the discrete calculations showing the impacts of the unconstrained sand column ($\bar{\rho} = 0.4$ and $\bar{v}_0 = 0.304$) against a stationary target. In this calculation the initial height to width ratio of the column was $H/W = 4$.

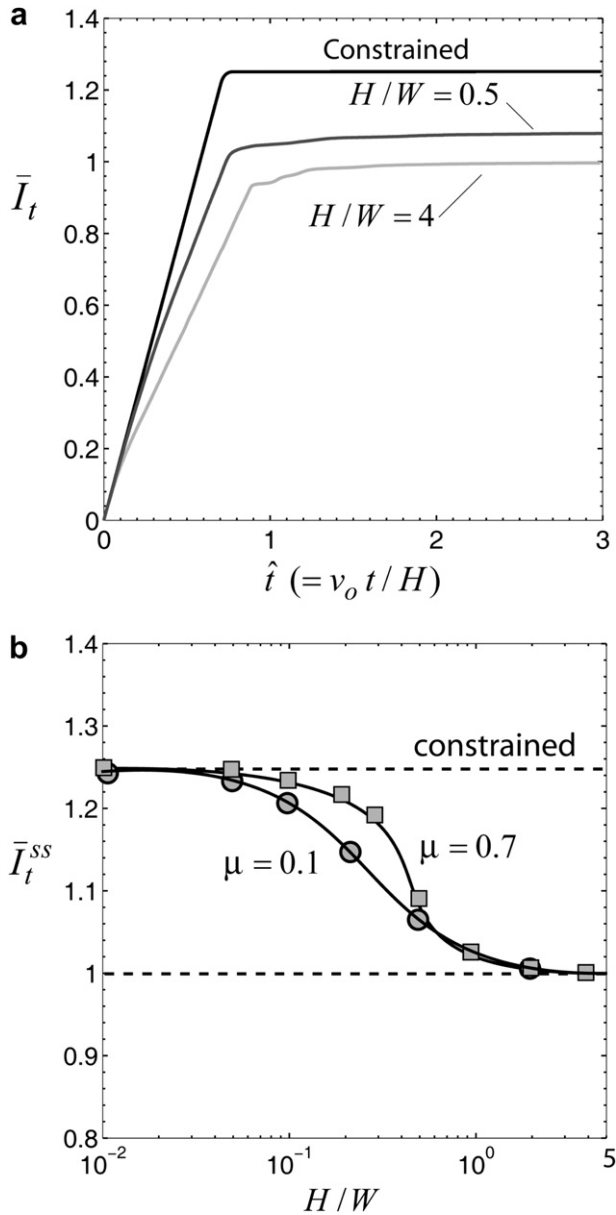


Fig. 19. (a) Predictions of the temporal dependence of the momentum transferred to a stationary target by sand columns with relative density $\bar{\rho} = 0.4$ travelling at $\bar{v}_0 = 0.304$. Results are shown for three values of the sand column aspect ratio H/W including the constrained limit corresponding to $H/W \rightarrow 0$. (b) The variation of \bar{I}_t^{SS} with H/W for a $\bar{\rho} = 0.2$ and $\bar{v}_0 = 0.304$ sand column impacting a stationary target. Results in (b) are included for two values of the co-efficient of friction μ between the particles.

Finally, we note that the foam analogy is not strictly applicable to the case of impact of the unconstrained sand column. However, the difference between the momentum transfer in the constrained and unconstrained cases is typically on the order to 10% and no larger than 30%. Given these relatively small differences, we argue that it suffices to use the foam model to obtain accurate estimates of the momentum transfer in nearly all situations involving the impact of sand columns against structures.

6. Concluding remarks

We have presented a discrete particle framework to investigate the interaction of an aggregate of particles travelling at high

velocities with rigid stationary and movable targets. The pressure exerted on the stationary target is shown to be mainly inertial and scales with $\bar{\rho}\bar{\rho}_s v_0^2$ where $\bar{\rho}$ and $\bar{\rho}_s$ are the relative density of the aggregate and density of the solid particles, respectively while v_0 is the velocity of the particles. The dependence on the interaction properties of the particles, viz. the co-efficient of restitution and co-efficient of friction between the particles, is shown to be negligible while there is a mild dependence on the contact stiffness K_n between particles. The momentum transferred to the movable target is mainly dependent on the ratio of the areal masses of the sand column and the target but also mildly dependent on $\bar{\rho}$ and K_n . For a wide range of conditions we demonstrate that the impact between the column and the target can be viewed as an inelastic collision between two bodies with an effective co-efficient of restitution ranging between 0 and 0.35.

The impact of a column of particles against the target is shown to be analogous to a foam impacting the target with the foam properties directly related to the properties of the aggregate including the density of the aggregate and the contact stiffness K_n . Consistent with observations from the discrete calculations, the foam properties are insensitive to the co-efficient of restitution and friction co-efficient between the particles. Both analytical and finite element (FE) solutions to this foam model are presented and are shown to be in excellent agreement with the discrete predictions. This foam analogy thus not only presents a numerically efficient method to solve the sand-structure interaction problem but also suggests that foam projectile loading might be a convenient analogue for studying this interaction within an experimental setting.

Acknowledgements

This research was supported by the Office of Naval Research (ONR grant number N00014-07-1-0764) as part of a Multidisciplinary University Research Initiative (David Shifler, Program manager).

Appendix A. Analysis of a metal foam impacting a rigid stationary target

The foam of density $\bar{\rho}\rho_s$ was modelled as a compressible continuum using the metal foam constitutive model of Deshpande and Fleck [32]. Write s_{ij} as the usual deviatoric stress and the von Mises effective stress as $\sigma_e \equiv \sqrt{3s_{ij}s_{ij}/2}$. Then, the isotropic yield surface for the metal foam is specified by

$$\hat{\sigma} - Y = 0, \quad (A1)$$

where the equivalent stress $\hat{\sigma}$ is a homogeneous function of σ_e and mean stress $\sigma_m \equiv \sigma_{kk}/3$ according to

$$\hat{\sigma}^2 \equiv \frac{1}{1 + (\alpha/3)^2} [\sigma_e^2 + \alpha^2 \sigma_m^2] \quad (A2)$$

The material parameter α denotes the ratio of deviatoric strength to hydrostatic strength, and the normalisation factor on the right hand side of Eq. (A2) is chosen such that $\hat{\sigma}$ denotes the stress in a uniaxial tension or compression test. An over-stress model is employed with the yield stress Y specified by

$$Y = \eta \dot{\epsilon}^p + \sigma_c \quad (A3)$$

in terms of the viscosity η and the plastic strain-rate $\dot{\epsilon}^p$ (work conjugate to $\hat{\sigma}$). The material characteristic $\sigma_c(\dot{\epsilon}^p)$ is the static uniaxial stress versus plastic strain relation of the foam. Normality

of plastic flow is assumed, and this implies that the “plastic Poisson’s ratio” $\nu_p = -\dot{\epsilon}_{22}^p / \dot{\epsilon}_{11}^p$ for uniaxial compression in the 1-direction is given by

$$\nu_p = \frac{1/2 - (\alpha/3)^2}{1 + (\alpha/3)^2}. \quad (\text{A4})$$

In the simulations, the foam is assumed to have a modulus E given by Eq. (16) and both the elastic Poisson’s ratio and plastic Poisson’s ratio vanish $\nu_p = \nu = 0$. Since the foam is used to model a loose aggregate of particles which has no static strength up to densification we assume a static strength of the form

$$\sigma_c = \begin{cases} \sigma_{pl} & \hat{\epsilon}^p \leq -\ln(1 - \epsilon_D) \\ \infty & \text{otherwise} \end{cases} \quad (\text{A5})$$

where ϵ_D is given by Eq. (12) and $\sigma_{pl} = \bar{\rho}\rho_s v_o^2 / 100$ (i.e. significantly less than the dynamic strength) in the calculations. (A strength equal to zero would cause numerical problems in the FE calculations.)

Radford et al. [33] have shown that the linear viscosity η results in a shock within the foam of width w given by

$$w = \frac{\eta \epsilon_D}{\bar{\rho}\rho_s v_o} \quad (\text{A6})$$

Using Eq. (A6), we choose a viscosity so that $w \ll H$ in all the calculations consistent with the discrete calculations that suggested that the shock width was no larger than about 10 particle diameters. We note in passing that similar to the discrete calculations Eq. (A6) predicts that the shock width decreases with increasing v_o and $\bar{\rho}$.

Finite element calculations using this constitutive description give predictions that are in line with the analytical results as well as consistent with the discrete particle predictions. However, the calculations differ on one count, viz. the FE calculations predict an initial transient with a high initial peak pressure as seen in Fig. 5b. We now demonstrate here that this initial transient is a consequence of the assumed viscosity.

Consider a foam column of semi-infinite extent with $\sigma_{pl} = 0$ and $E \rightarrow \infty$ impacting at $t = 0$ a rigid stationary wall at $x = 0$. As shown in Section 3.5, the steady-state pressure exerted on the wall is given by Eq. (15). Here we attempt to develop a relation for the initial transient before this steady-state pressure is attained. Given that the foam has $\nu_p = 0$ and undergoes no lateral expansion, the problem reduces to a one-dimension (1D). The 1D equilibrium equation for the compressive stress σ in the x -direction is

$$\frac{\partial \sigma}{\partial x} = \rho \frac{\partial v}{\partial t} \quad (\text{A7})$$

where $\rho = \bar{\rho}\rho_s$ and v the particle velocity. Substituting the constitutive relation

$$\sigma = \eta \frac{\partial v}{\partial x} \quad (\text{A8})$$

in Eq. (A7) we get

$$\frac{\partial v}{\partial t} = \kappa \frac{\partial^2 v}{\partial x^2} \quad (\text{A9})$$

where $\kappa = \eta / \rho$. The solution to this equation with initial conditions $v = v_o$ at $t = 0$ and $v = 0$ at $x = 0$ is

$$v = v_o \operatorname{erf}\left(\frac{x}{2\sqrt{\kappa t}}\right) \quad (\text{A10})$$

The pressure p exerted on the wall is $\sigma(x = 0)$ and follows from Eq. (A8) as

$$p = v_o \sqrt{\frac{\eta \rho}{\kappa t}}. \quad (\text{A11})$$

This relation is valid provided the strain ϵ at $x = 0$ is less than ϵ_D . Now the strain-rate $\dot{\epsilon}$ is given by $\partial v / \partial x$ with $v(x)$ stipulated in Eq. (A10). Consequently,

$$\dot{\epsilon}(x = 0, t) = \frac{v_o}{\sqrt{\pi \kappa t}} \quad (\text{A12})$$

and

$$\epsilon(x = 0, t) = 2v_o \sqrt{\frac{t}{\pi \kappa}} \quad (\text{A13})$$

The time t_c until when Eq. (A11) is valid then follows by setting $\epsilon = \epsilon_D$ in Eq. (A13) to give

$$t_c = \frac{\epsilon_D^2}{4v_o^2} \frac{\eta \pi}{\rho} \quad (\text{A14})$$

The pressure p reduces from $p = \infty$ at $t = 0$ to

$$p = \frac{2\rho v_o^2}{\pi \epsilon_D} \quad (\text{A15})$$

at $t = t_c$. Subsequently, it will rise to its steady-state value of $\rho v_o^2 / \epsilon_D$. This analysis shows that the initial transient seen in Fig. 5b is due to the finite viscosity η .

References

- [1] Fleck NA, Deshpande VS. The resistance of clamped sandwich beams to shock loading. *Journal of Applied Mechanics* 2004;71:386–401.
- [2] Liang Y, Spuskanyuk AV, Flores SE, Hayhurst DR, Hutchinson JW, McMeeking RM, Evans AG. The response of metallic sandwich panels to water blast. *Journal of Applied Mechanics* 2007;74:81–99.
- [3] Deshpande VS, Heaver A, Fleck NA. An underwater shock simulator. *Proceedings of the Royal Society of London* 2006;A462:1021–41.
- [4] Wei Z, Dharmasena KP, Wadley HNG, Evans AG. Analysis and interpretation of a test for characterizing the response of sandwich panels to water blast. *International Journal of Impact Engineering* 2007;34:1602–18.
- [5] Bergeron D, Walker R, Coffey C. Detonation of 100-gram anti-personnel mine surrogate charges in sand-A test case for computer code validation. Suffield Report No. 668. Ralston, Alberta, Canada: Defence Research Establishment Suffield; 1998.
- [6] Braid MP. Experimental investigation and analysis of the effects of anti-personnel landmine blasts. Canada: Defence Research Establishment Suffield; 2001. Special Publication, DRES SSSP 2001-188.
- [7] Weckert S, Andersen C. A Preliminary comparison between TNT and PE4 landmines. Report no. DSTO-TN-0723. Edinburgh, South Australia: Defence Science and Technology Organization; 2006.
- [8] Westine PS, Morris BL, Cox PA, Polch E. Development of computer program for floor plate response from land mine explosions; 1985. Contract Report No. 1345 for U.S. Army TACOM Research and Development Centre.
- [9] Morris BL. Analysis of improved crew survivability in light vehicles subjected to mine blast; 1993. Final report for contract no. DAAK70-92-C-0058 for the U.S. Army Belvoir RDEC, Ft. Belvoir, VA.
- [10] Johnson SM. Explosive excavation technology. NCG report no. 21. Livermore, USA: US army Engineer Nuclear cratering group; 1971.
- [11] Grujicic M, Pandurangan B, Cheeseman BA. The effect of degree of saturation of sand on detonation phenomena associated with shallow-buried and ground-laid mines. *Journal of Shock and Vibration* 2006;13:41–61.
- [12] Grujicic M, Pandurangan B, Qiao R, Cheeseman BA, Roy WN, Skaggs RR, et al. Parameterization of the porous-material model for sand with different levels of water saturation. *Soil Dynamics and Earthquake Engineering* 2008;28:20–35.
- [13] Wang Z, Hao H, Lu Y. A three-phase soil model for simulating stress wave propagation due to blast loading. *International Journal for Numerical and Analytical Methods in Geomechanics* 2004;28:33–56.
- [14] Wang Z, Lu Y. Numerical analysis on dynamic deformation mechanisms of soils under blast loading. *Soil Dynamics and Earthquake Engineering* 2003;23:705–14.
- [15] Drucker DC, Prager W. Soil mechanics and plastic analysis or limit design. *Quarterly of Applied Mathematics* 1952;10:157–65.

- [16] Laine P, Sandvik A. Derivation of mechanical properties for sand. In: Proceedings of the 4th Asia-Pacific Conference on shock and impact loads on structures. Singapore: CI-Premier PTE LTD; 2001. p. 361–8.
- [17] Tremblay JE, Bergeron DM, Gonzalez R. Protection of soft-skinned vehicle occupants from landmine effects; 1998. The Technical Cooperation Program, Subcommittee on Conventional Weapons Technology, Technical Panel W-1, USA.
- [18] Wang J. Simulation of a landmine explosion using LS-DYNA3D software. Australia: Department of Defence; 2001. DSTO-TR1168.
- [19] Deshpande VS, McMeeking RM, Wadley HNG, Evans AG. Constitutive model for predicting dynamic interactions between soil ejecta and structural panels. *Journal of Mechanics and Physics of Solids* 2009;57:1139–64.
- [20] Bagnold RA. Experiments on a gravity-free dispersion of large solid particles in a Newtonian fluid under shear. *Proceedings of the Royal Society, London* 1954;A225:49–63.
- [21] Taylor GI. The pressure and impulse of submarine explosion waves on plates. *The Scientific Papers of Sir Geoffrey Ingram Taylor*. In: Batchelor G, editor. *Aerodynamics and the mechanics of projectiles and explosions*, vol. III. Cambridge, UK: Cambridge University Press; 1963. p. 287–303.
- [22] Plimpton S. Fast parallel algorithms for short-range molecular dynamics. *Journal of Computational Physics* 1995;117:1–19.
- [23] Cundall PA, Strack ODL. A discrete numerical model for granular assemblies. *Geotechnique* 1979;29:47–65.
- [24] Campbell CS, Brennen CE. Chute flows of granular material: some computer simulations. *Journal of Applied Mechanics, ASME* 1985;52:172–8.
- [25] Campbell CS. Granular shear flows at the elastic limit. *Journal of Fluid Mechanics* 2002;465:261–91.
- [26] Bathurst RJ, Rothenburg L. Micromechanical aspects of isotropic granular assemblies with linear contact interactions. *Journal of Applied Mechanics, ASME* 1988;55:17–23.
- [27] Silbert LE, Ertaş D, Grest GS, Halsey TC, Levine D, Plimpton SJ. Granular flow down an inclined plane: Bagnold scaling and rheology. *Physics Review* 2001;E 64:051302.
- [28] Reid SR, Peng C. Dynamic uniaxial crushing of wood. *International Journal of Impact Engineering* 1997;19:531–70.
- [29] Tan PJ, Reid SR, Harrigan JJ, Zou Z, Li S. Dynamic compressive strength properties of aluminium foams. Part II – shock theory and comparison with experimental data. *Journal of Mechanics and Physics of Solids* 2005;53: 2206–30.
- [30] Deshpande VS, Fleck NA. One dimensional response of sandwich plates to underwater shock loading. *Journal of Mechanics and Physics of Solids* 2004; 53:2347–83.
- [31] Gibson LJ, Ashby MF. *Cellular solids: structures and properties*. 2nd ed. Cambridge, UK: Cambridge University Press; 1997.
- [32] Deshpande VS, Fleck NA. Isotropic constitutive models for metallic foams. *Journal of Mechanics and Physics of Solids* 2000;48:1253–83.
- [33] Radford DD, Deshpande VS, Fleck NA. The use of metal foam projectiles to simulate shock loading on structures. *International Journal of Impact Engineering* 2005;31:1152–71.